Pyrolysis temperature dependence of sodium storage mechanism in non-graphitizing carbons

Hélène Tonnoir, Da Huo, Carine Davoisne, Alain Celzard, Vanessa Fierro, Damien Saurel, Mimoun El Marssi, Manal Benyoussef, Philippe Meunier, Raphaël Janot

Pyrolysis temperature dependence of sodium storage mechanism in non-graphitizing carbons

Hélène TONNOIR [a], Da HUO [a], Carine DAVOISNE [a], Alain CELZARD [b,c], Vanessa FIERRO [b], Damien SAUREL [d], Mimoun EL MARSSI [e], Manal BENYOUSSEF [e], Philippe MEUNIER [f], Raphaël JANOT [a,*]

[a] Laboratoire de Réactivité et Chimie des Solides (LRCS), CNRS UMR7314, Université de Picardie Jules Verne, 15 Rue Baudelocque, 80039 Amiens Cedex 1, France,

[b] Université de Lorraine, CNRS, IJL, F-88000 Epinal, France

[c] Institut Universitaire de France (IUF)

[d] Center for Cooperative Research on Alternative Energies (CIC energiGUNE), Basque Research and Technology Alliance (BRTA), Parque Tecnológico de Álava, Albert Einstein, 48, 01510, Vitoria-Gasteiz, Spain

[e] Laboratoire de Physique de la Matière Condensée (LPMC), UPJV UR2081, Université de Picardie Jules Verne, 33 rue Saint Leu, 80039 Amiens Cedex 1, France

[f] MERSEN France Gennevilliers, 41 rue Jean Jaurès, 92231 Gennevilliers Cedex, France

*Corresponding author. Tel: +(33)3.22.82.57.77. E-mail: raphael.janot@u-picardie.fr

Abstract

Hard carbons are the most investigated materials as negative electrode for Na-ion batteries, although the exact mechanism of sodium storage remains under debate. This work is focused on the study of the sodiation mechanism of non-graphitizing carbons (NGC) prepared in a wide range of pyrolysis temperatures (1000 °C to 2500 °C), thus covering the whole range from hard carbons (HC) to glassy carbons (GC). Structural and textural characterizations show that increasing the pyrolysis temperature leads to NGCs with a more ordered structure, containing fewer heteroatoms and structural defects, and particularly leads to a developed closed microporosity. In this work, *in situ* Raman spectroscopy at different excitation wavelengths is used to clarify the mechanism of electrochemical sodiation: it is revealed that the intercalation of Na^+ between the graphene layers occurs mainly during the sloping part of the galvanostatic profile, whereas the plateau at low voltage (below 0.1 V vs. Na^+/Na) can be associated with the filling of micropores with sodium.

Keywords: Hard carbon, Sodium-ion battery, SAXS, Porosity, *In situ* Raman spectroscopy

1. Introduction

The recent reports of the Intergovernmental Panel on Climate Change (IPCC, United Nations, August 2021, February and April 2022) [1–3] emphasize the urgency of reducing greenhouse gas emissions to limit global warming. In this context, the massive development of renewable energy sources appears as a necessity, but being intermittent, the use of efficient energy storage devices is required for mobile and stationary applications.[4] Thus, the development of energy storage systems will play a major role in the upcoming energy transition.[5] Among all the storage devices that can be used, electrochemical storage by batteries appears as an efficient and reliable way to store energy.

Lithium-ion batteries (LIBs) are considered as one of the most powerful battery technologies, but they require the use of expensive raw materials.[6] Sodium-ion batteries (SIBs) are then considered a promising alternative to LIBs. Indeed, sodium shows similar

properties to lithium, while being more abundant, evenly distributed on Earth and less expensive.[6–9] Moreover, costs of SIBs can be significantly reduced by the use of Al current collector for both electrodes.[10] Nevertheless, the energy density of SIBs remains today low compared to LIBs, and SIBs still require optimizations of their components (*i.e.*, electrodes and electrolyte).[10] Graphite, the commonly used negative electrode material for LIBs (with a theoretical specific capacity of 372 mAh/g), is unsuitable for SIBs using common carbonate electrolytes, with sodium showing poor intercalation into graphite (*i.e.*, formation of a stage 8 compound, NaC_{64}) leading to a low electrochemical capacity of about 35 mAh/g.[11–13] Several other materials, such as metal oxides,[14–19] alloy-based materials,[20–22] organic compounds [23–27] or other carbonaceous materials,[28–35] have been studied as anode materials for SIBs. With reversible capacities up to 300 mAh/g, low working potential vs Na^+/Na and good cycling stability, hard carbons (HC) appear to be the best candidates.[36–39]

Hard carbons are non-graphitizable carbons composed of disorganized and randomly oriented turbostratic nano-sized domains (*i.e.*, BSUs = basic structural units). Such materials show high microporosity (*i.e.*, pore size less than 2 nm).[8,9] They can be obtained from the pyrolysis of various precursors such as sucrose,[9,40,41] glucose,[11,34,42] cellulose,[38,43,44] lignin,[7] phenolic resins,[45–48] pre-oxidized pitch [39,49] and various biomass residues.[50–54] These carbons are generally obtained at pyrolysis temperatures above 1000 °C and cannot be converted into graphitic carbons by high-temperature treatment. When hard carbons are synthesized at very high temperature (typically 2500 °C and above), they are often called glassy carbons (GCs).[55] This is due to the glass-like aspect that these carbons present, prior to milling, when prepared from bulk thermosetting resins (*e.g.*, phenolic) cast in molds with a smooth surface.[56–58]

Since the development of the metal-ion batteries, many studies have tried to identify the electrochemical storage mechanism of Na^+ in non-graphitizing carbons (NGC). The galvanostatic discharge profile of NGCs versus Na^+/Na can be decomposed into two parts: a sloping part from the Open Circuit Voltage (OCV; around 2.5 V) down to 0.1 V, and a low-potential plateau under 0.1 V. The first hypothesis for the mechanism of sodium storage in HCs was presented in 2000 by Stevens and Dahn.[34] By studying HCs prepared by pyrolysis of glucose at 1000 °C and 1150 °C, they concluded that the storage mechanisms of lithium and sodium ions are the same: the sloping part is associated with the intercalation of sodium ions between graphene layers in the turbostratic domains, and the plateau region is associated with the filling of nanopores. They then confirmed their first proposed mechanism using *in situ*

Wide-Angle X-Ray Scattering (WAXS) and *in situ* Small Angle X-Ray Scattering (SAXS).[11,59] However, in 2015, Bommier *et al*.[9] presented an alternative mechanism for which the sloping part is associated with the adsorption of sodium ions onto structural defects in the carbon, and the plateau region is associated with the intercalation of sodium between graphene layers in the turbostratic domains. They used commercial glassy carbons as well as hard carbons prepared from sucrose pyrolyzed at 1100 °C, 1400 °C and 1600 °C, characterized by Galvanostatic Intermittent Titration Technique (GITT) and *ex situ* X-Ray Diffraction (XRD).

Since then, numerous studies have been published on the storage mechanism of sodium ions in hard carbons, without any scientific consensus until now, due to many contradictions between the results from different characterization techniques and the complexity of the hard carbons microstructure.[6,60] As an example of the inconsistent conclusions that can be obtained using the same characterization method, *operando* ^{23}Na solid-state Nuclear Magnetic Resonance (NMR) and *ex situ* ^{23}Na Magic-Angle Spinning solid-state Nuclear Magnetic Resonance (MAS NMR) were used in 2016 by Stratford *et al*.[61] in order to investigate the storage mechanism of sodium in a commercial HC. They concluded that a two-stage mechanism was occurring and that the plateau region was due to Na filling the HC micropores, which tends to confirm the intercalation-pore filling mechanism proposed firstly by Stevens and Dahn. On the contrary, in 2017, *ex situ* ^{23}Na MAS NMR experiments performed on cellulose-based HCs pyrolyzed between 900 °C and 1500 °C by Qiu *et al*.[62] led them to the conclusion that the intercalation of Na^+ between graphene layers occurs in the plateau region. Thus, the mechanism they proposed is the same as the one proposed by Bommier *et al*.: adsorption on the slope, intercalation on the plateau. Finally, in 2020, Au *et al*.[63] used *ex situ* ^{23}Na MAS NMR on HCs prepared by hydrothermal carbonization of glucose and subsequent heat treatments between 1000 °C and 1900 °C. Their conclusion was that the plateau region was related to pore filling by Na, in agreement with the observations made by Stratford *et al*. Many other characterization techniques have been used to study the sodiation mechanism of HCs, such as Raman spectroscopy,[64,65] *ex situ* electrochemical dilatometry [66] or ex-situ X-ray Photoelectron Spectroscopy (XPS) [7] without reaching a definite conclusion on the mechanism.

In this study, a focus is made on electrochemical tests coupled with Raman spectroscopy which already appeared as a very powerful technique for mechanistic studies in HCs in the literature. In 2018, Reddy *et al*. [64] conducted *operando* Raman measurements with a 632.8

nm excitation source to investigate the storage mechanism of sodium in a coconut shell-based HC. The G band shifted from ~ 1600 cm^{-1} to ~ 1550 cm^{-1} in the sloping part due to the intercalation of Na between the graphene layers, while there was no further change in the position of the G band in the plateau region. A four-step mechanism was proposed: adsorption onto the active sites of the surface, intercalation between the graphene layers, first at the defects, then at the rest of the layer, and finally filling of the micropores. In 2020, Weaving *et al*.[65] used *operando* Raman spectroscopy at 532 nm on a commercial plant-based HC and also concluded that there was an intercalation-pore filling mechanism. These two studies highlighted that *in situ*/*operando* Raman spectroscopy represents a valuable tool to elucidate the sodiation mechanism in hard carbons. So far, however, the influence of the excitation wavelength on Raman scattering during HC sodiation has been little discussed.

Although the mechanism of sodium storage in HCs is still under debate, most studies agree on three phenomena involved in sodium storage: Na^+ adsorption on structural defects, intercalation between graphene layers, and micropore filling.[6] The debate lies in the voltage range at which each of these mechanisms prevails.

The aim of the present study was therefore to develop a deeper understanding of the sodiation mechanism in NGCs using commercial carbons prepared over an extended temperature range (1000 °C - 2500 °C), to cover the whole range from hard carbons (HC) to glassy carbons (GC). Being vitreous, these materials are known to exhibit a low amount of heteroatoms, even at low pyrolysis temperature. In our work, several characterization techniques were used to precisely study the structure, texture and electrochemical performance of NGCs. Then, *in situ* Raman spectroscopy measurements with three different excitation wavelengths were carried out to investigate the structural evolution during the discharge process (*i.e.*, sodiation).

2. Materials and methods

2.1. *Materials used*

For this study, glassy carbon crucibles were supplied by Mersen. They were pyrolyzed at 1000 °C, 1500 °C, 2000 °C and 2500 °C. The four materials were then ground using an agate

mortar and sieved to 20 µm. The powdered carbons thus obtained will be referred to as NGCX (X being the temperature of pyrolysis).

2.2. *Structural and textural characterizations*

X-Ray Diffraction (XRD) measurements were performed in Bragg-Brentano configuration for 2θ diffraction angles between 10 ° and 80 ° with a Bruker AXS D8 Advance diffractometer using a copper X-ray source ($\lambda_{K\alpha}$ = 0.15418 nm). A shallow sample holder with a zero-background single crystal Si plate was used to minimize sample transparency. The XRD patterns were analyzed using the model developed by Mallet-Ladeira.[67] The average lateral size of the graphene domains L_a and the average thickness of the graphene layers stacking L_c were determined using Sherrer's formula from the (10l) and (002) reflections, respectively.

Raman spectroscopy was performed using a Renishaw inVia Qontor confocal Raman microscope for the excitation wavelengths of 532 nm and 633 nm, and a ThermoScientific DXR Raman microscope for the excitation wavelength of 780 nm. The power of the laser was set to low values (~ 1 mW) to avoid local heating of the sample. Ten spectra were recorded for each sample and two acquisitions of 30 s were made for each spectrum. The Raman spectra were analyzed using the model developed by Mallet-Ladeira,[67] and the average lateral size L_a of the graphene domains was calculated using the same model.[68] The quantification of structural defects was achieved using the ratio of the integrated areas A_D/A_G of the D and G bands.

Elemental analysis of the carbons was performed with a Thermofisher Flash EA 1112 apparatus. The combustion was done at 950 °C.

Transmission Electron Microscopy (TEM) was performed with a FEI Tecnai F20-S-TWIN microscope using an acceleration voltage of 200 kV, equipped with a GIF Tridiem from Gatan. For the microstructural investigation, sample preparation was done by suspending the powder in ethanol. Then, one or two drops of the suspension were deposited on a copper grid with a holey carbon film. High-resolution imaging (HRTEM) was performed by controlling the electron dose in order to avoid artefacts induced by the electron beam. The d-spacing of the graphene layer in the different sample was obtained by Fast Fourier Transform (FFT) on the HRTEM images.

Textural properties of the carbons were evaluated with nitrogen and hydrogen adsorption isotherms at -196 °C using a Micromeritics ASAP 2020 automatic manometric

device. Carbon samples were outgassed under secondary vacuum at 110 °C for at least 48h. The specific surface area was determined either from N_2 isotherms by applying the Brunauer, Emett and Teller (BET) equation to obtain A_{BET} (m^2/g), or from both N_2 and H_2 isotherms by applying the two-dimensional Non-Local Density Functional Theory (2D-NLDFT) to obtain $S_{2D\text{-}NLDFT}$ (m^2/g) using the SAIEUS software supplied by Micromeritics, which also allows to determine the pore size distribution (PSD).[69] The integration of the PSD in the adequate pore diameter range allowed the determination of the volumes of micropores (< 2 nm), V_μ (cm^3/g), mesopores (2−50 nm), V_{meso} (cm^3/g) and the total pore volume, V_{tot} (cm^3/g).

The skeletal density of the carbons was measured using a Micromeritics AccuPyc1330 helium pycnometer. The 1 cm^3 chamber was flushed with twenty He purges to remove air from the chamber and the carbon surface, and then five measurements were recorded.

Small-Angle X-Ray Scattering (SAXS) was performed using a Bruker Nanostar instrument equipped with a Vantec 2000 2D detector. Three sample-to-detector distances were used to cover the range 0.1-30 nm^{-1}. The instrument was calibrated in intensity, and the SAXS patterns were corrected for self-absorption, transmission, background signal, detector distortion, and detector efficiency as described in [70]. Pore size, inter-pore distance and surface area were determined by fitting the SAXS patterns to the model developed in [70], based on the Teubner-Strey model applied to micropores.

2.3. *Electrochemistry*

2.3.1. Electrode formulation

The slurries were made in an aqueous formulation using carboxymethyl cellulose (Na-CMC, Acros Organics, average molar mass 700 000 g/mol), carbon black C45 (Imerys) and Triton X-100 (Tx100, Sigma-Aldrich) as polymeric binder, conductive additive and surfactant, respectively. The following composition, expressed in weight percent (wt%), was used: 92 wt% NGC / 2.6 wt% CMC / 2.9 wt% C45 / 2.5 wt% Tx100. The slurries were then homogenized with a magnetic stirrer for 5 h, and then coated on an aluminum foil (20 µm thick) using a doctor blade (300 µm gap). After coating, the films were dried at 100 °C for 1 h before cooling to room temperature overnight. Electrodes of 15 mm diameter were then punched and dried overnight at 110 °C under vacuum in a Büchi glass oven. The mass loading of active material was approximately 3 mg/cm^2 for all samples.

2.3.2. Galvanostatic cycling

Electrochemical studies were carried out in two-electrode coin-cells (CR2032) using NGC as the working electrode, sodium metal (Sigma-Aldrich) as the counter and reference electrode, glass fiber separator (Whatman), and a molar solution of sodium hexafluorophosphate ($NaPF_6$, Stella Chemicals) in a mixture of ethylene carbonate and dimethyl carbonate (EC/DMC, DodoChem, 50:50 mass) as the electrolyte (NP30). The coin cells were assembled in a glovebox under argon atmosphere. They were then cycled between 0 V and 2.5 V (vs Na^+/Na) at C/20 (18.6 mA/g_{carbon}, calculated considering the hypothetical formation of a NaC_6 phase during sodiation with a theoretical specific capacity of 372 mAh/g) for 10 cycles and, then, at C/10 for 100 cycles. A rate of C/n corresponds to the insertion of one Na^+ ion into the carbon, for 6 carbon atoms, in n hours.

2.4. *In situ Raman spectroscopy*

To perform *in situ* Raman measurements, self-supported electrodes were formulated in an aqueous slurry with the following formulation: 82.5 wt% NGC / 15 wt% CMC / 2.5 wt% Tx100. To avoid possible contribution from carbon black sodiation, no conductive additive was used. The slurry was stirred for 5 h. Then, electrodes of approximately 14 mm diameter were deposited on a Mylar sheet, peeled off from the Mylar substrate after drying at room temperature, and dried overnight at 110 °C in a Büchi glass oven. The next step was to assemble the two-electrode coin cell (CR2032) in a glovebox using the self-supported NGC electrode as the working electrode. A 2 mm-diameter hole was punched on the top cover of the coin cell before assembly. It was then closed by a thin glass window bonded with an epoxy adhesive (Loctite EA9492, Henkel) just after the coin cell was crimped to ensure the airtightness of the cell. The electrochemical cell and the cycling support used are described in Figure S1.

The cells were then discharged at C/50 and stopped at targeted potential values between OCV and 0 V (cf. Figure S2). After relaxation to steady states, Raman spectra were recorded at different points on the sample using excitation wavelengths of 532 nm, 633 nm or 780 nm. The Raman spectra were analyzed as described in section 2.2.

3. Results and discussion

3.1. *Impact of the pyrolysis temperature on the NGC properties*

3.1.1. Structural and textural properties

The XRD patterns of the four samples NGC1000, NGC1500, NGC2000 and NGC2500 are shown in Figure 1a. The patterns are typical of non-graphitic carbons with a broad (002) reflection at around 2θ = 23 ° related with the interplanar distance between the graphene layers in the turbostratic domains, and a broad and asymmetric (10l) peak at around 2θ = 45 ° associated with the contributions from the (100), (101) and (004) reflections.[6] With the increase in pyrolysis temperature, (002) becomes sharper and (004) is more visible. For NGC2500, a sharp peak is observed at 2θ = 26 ° due to the presence of a more ordered second phase ($d_{(002)}$ = 0.345 nm (cf. Table 1)), close to the $d_{(002)}$ value for an ideal turbostratic stacking, which is 0.344 nm).[71] Thus, the structure of the NGCs becomes more ordered as the pyrolysis temperature increases. This is confirmed by a decrease in the average $d_{(002)}$ value as the pyrolysis temperature increases, from 0.369 nm for NGC1000 to about 0.349 nm for NGC2500 (cf. Table 1).

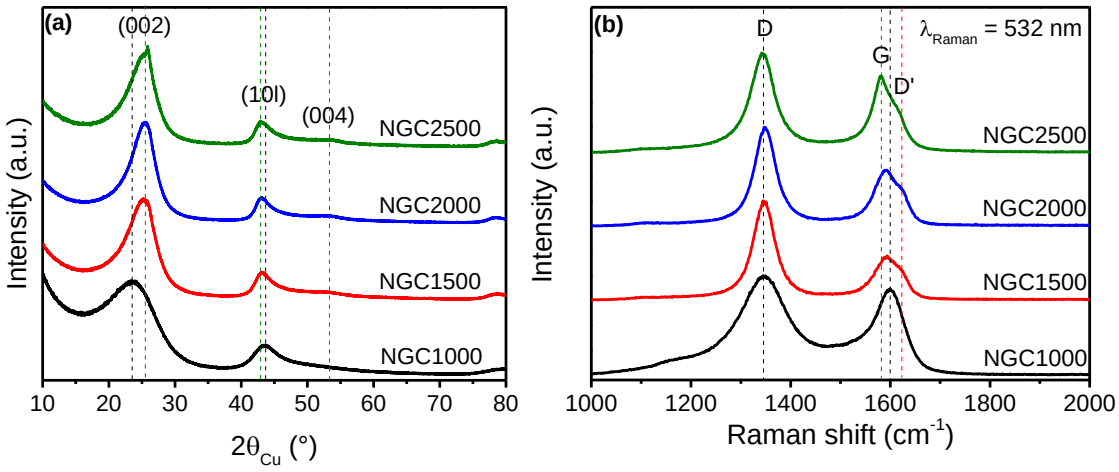

Fig. 1. (a) XRD patterns and (b) Raman spectra (λ_{Raman} = 532 nm) of non-graphitizing carbons pyrolyzed at different temperatures.

Table 1. Structural characteristics of NGCs.

Sample		NGC1000	NGC1500	NGC2000	NGC2500
XRD	L_a (nm)	3.70 ± 0.03	8.53 ± 0.18	8.52 ± 0.18	8.52 ± 0.18
	L_c (nm)	1.16 ± 0.01	1.71 ± 0.02	1.98 ± 0.02	1.76 ± 0.02
	$d_{(002)}$ (nm)	0.369 ± 0.001	0.357 ± 0.001	0.354 ± 0.001	0.352/0.345 ± 0.001
TEM	$d_{(002)}$ (nm)	0.382 ± 0.030	0.353 ± 0.012	0.352 ± 0.019	0.352 ± 0.023
Raman Spectroscopy (532 nm)	L_a (nm)	6.4 ± 0.3	8.7 ± 0.4	9.4 ± 0.2	9.3 ± 0.6
	A_D/A_G	2.0 ± 0.1	3.2 ± 0.4	2.6 ± 0.2	2.4 ± 0.1
	$A_{D'}/A_G$		0.6 ± 0.1	0.7 ± 0.1	0.7 ± 0.1
	$A_{D+D'}/A_G$	2.0 ± 0.1	3.8 ± 0.5	3.3 ± 0.2	3.1 ± 0.2

The evolution of the composition of the carbonaceous materials with the increase in pyrolysis temperature was investigated by elemental analysis (cf. Table 2). As the pyrolysis temperature increases, the amount of heteroatoms such as H, O or N decreases. Above 2000 °C, the contents of hydrogen, oxygen and nitrogen are below the detection limit (< 0.05 wt%). The evolution of the hydrogen content in the structure gives information on the amount of C-H bonds. Usually, these bonds are located at the edges of graphene layers. Thus, as the pyrolysis temperature increases, the hydrogen content decreases (from 4.67 at% to 0), which means that the amount of graphene edges decreases.

Figure 1b presents the first-order Raman spectra obtained for the laser excitation wavelength of 532 nm for the four NGCs. All the spectra present two bands: the D band around 1350 cm^{-1}, associated with structural defects of the material, and the G band around 1600 cm^{-1}, originating from in-plane vibrations of sp^2 C atoms. For a pyrolysis temperature above 1500 °C, another band appears around 1615 cm^{-1} as a shoulder of the G band. This can be correlated with the presence of a D' band as explained by Puech *et al.*[72] For small crystallite sizes (L_a < 7 nm), the G and D' bands merge into a single band. This agrees well with the value of L_a, average lateral size of the graphitic domains reported in Table 1. For NGC1000, L_a is equal to ~ 6.4 nm while it increases to ~ 8.7 nm for NGC1500 and keeps increasing at higher temperatures. The A_D/A_G ratio of the integrated areas increases from 2.0 to 3.2 for pyrolysis temperatures of 1000 °C and 1500 °C, respectively, and then decreases for higher temperatures (2.6 for NGC2000 and 2.4 for NGC2500) while $A_{D'}/A_G$ remains fairly constant for NGC1500, NGC2000 and NGC2500. Thus, the amount of structural defects first increases with the

pyrolysis temperature and then decreases for temperature above 1500 °C. Moreover, for NGC2500, the more turbostratic particles were also observed by Raman spectroscopy. These turbostratic particles have sharper D and G bands and an A_D/A_G ratio of 2.2.

Table 2. Evolution of the composition of the non-graphitizing carbons with the increase of pyrolysis temperature.

Sample	C (wt%) [at%]	H (wt%) [at%]	O (wt%) [at%]	N (wt%) [at%]
NGC1000	97.59 [94.87]	0.40 [4.67]	0.52 [0.38]	0.10 [0.08]
NGC1500	96.00 [98.18]	0.14 [1.72]	0.03 [0.02]	<0.05
NGC2000	93.51 [100]	<0.05	<0.05	<0.05
NGC2500	98.56 [100]	<0.05	<0.05	<0.05

Raman spectroscopy was also performed at higher excitation wavelengths (633 nm and 780 nm) for the four NGCs (cf. Figure 2a and Figure S3). It should be noted that as the laser wavelength increases (from 532 to 780 nm), a blue shift is observed for the D band, whereas no shift is noticed for the G band. Regarding the D' band, no shift could be evidenced. These results are consistent with the previous results of Puech *et al*. showing a shift of the D band.[72] At some point (780 nm), a merging between the G and D' bands can be observed. The evolution of the D band position as a function of laser energy was fitted by a linear regression for each sample (Figure 2b). The parameters obtained for the fits are presented in Table S1. For all samples, the D-band is linearly shifted with a rate of about 50 cm^{-1}/eV: 55 cm^{-1}/eV for NGC1000; 51 cm^{-1}/eV for NGC1500 and NGC2000; and 48 cm^{-1}/eV for NGC2500. Mallet-Ladeira *et al.*[68] compared cokes and pyrocarbons with different crystallite sizes L_a, obtained at different pyrolysis temperatures. They observed that the rate of the D band shift decreased as the pyrolysis temperature and L_a increased. The same phenomenon is observed, here, for the

NGC samples. Indeed, Raman spectroscopy showed that L_a increases with the increase of the pyrolysis temperature. Moreover, the shift of the D band is in agreement with the observations of Merlen *et al.*,[73] who explained this phenomenon as a double resonance mechanism behind the D band in Raman spectroscopy, first demonstrated by Thomsen *et al.*[74]

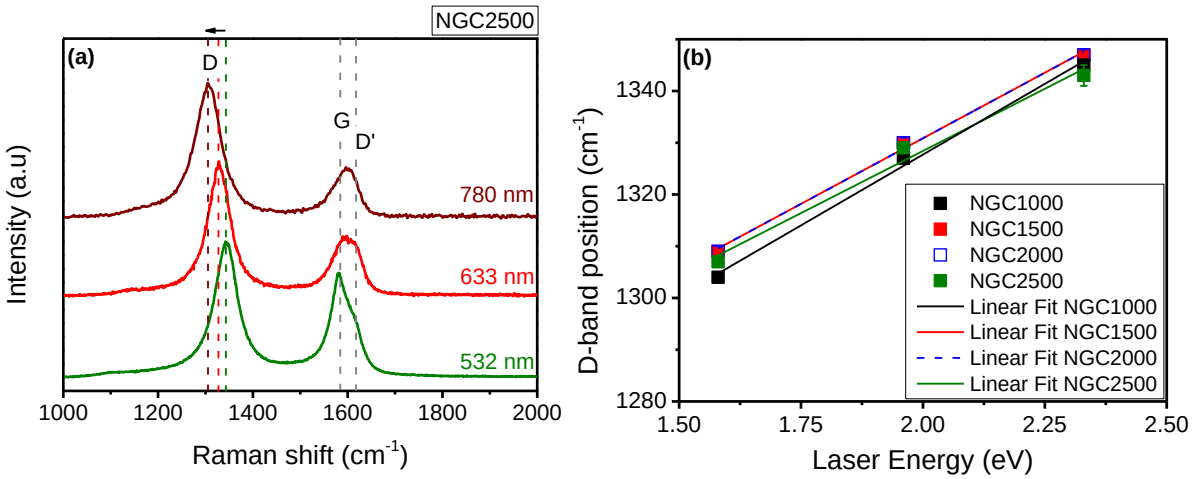

Fig. 2. (a) Raman spectra at different laser wavelengths for NGC2500 and (b) Evolution of the D band position with the increase of the laser energy.

Moreover, it is observed that the intensity of the G band decreases as the wavelength increases while D and D' bands seem to remain similar (Figure 2a). The $A_{D+D'}/A_G$ ratios are different (Table S2), while for each sample, the width of the G band remains constant, for all excitation wavelengths. This confirms the previous findings of Mallet *et al.*[68] that the half-width at half maximum (HWHM) of the G band is a relevant indicator for determining L_a.

Figure S4 shows the evolution of $\log(A_{D+D'}/A_G)$ as a function of $\log(E_{laser})$. This evolution was also fitted using a linear function for each sample. For all samples, a decrease in $\log(A_{D+D'}/A_G)$ is observed as $\log(E_{laser})$ increases (*i.e.*, as the laser energy increases). The parameters obtained for the fits are presented in Table S3. Thus, $A_{D+D'}/A_G$ is proportional to the laser energy to the power of *a* (*a* being the slope of the linear fit, which is negative since $A_{D+D'}/A_G$ is inversely proportional to energy). For NGC1000, $A_{D+D'}/A_G$ is proportional to $E_{laser}^{-1.7}$, and the value of *a* decreases to -2.9 for pyrolysis temperatures above 1500 °C (-2.9 for NGC1500 and NGC2500, -2.4 for NGC2000). For graphene and nanographite, the value of *a* can reach –4, according to the literature [75,76]. The tendency observed in our study is similar

to those reported by Mallet-Ladeira *et al*.[68] for cokes and pyrocarbons, showing that *a* decreases when the pyrolysis temperature and L_a increase.

Both XRD and Raman spectroscopy showed that the structural order in the material increases when the pyrolysis temperature increases. TEM was performed on the four NGCs in order to visualize the evolution of the nanostructure when the pyrolysis temperature increases (cf. Figure 3). The TEM images show the microstructural changes that occur as the pyrolysis temperature increases. For NGC1000, the material shows a lot of disorder with randomly oriented carbon sheets. A relatively small amount of turbostratic domains can be identified (see orange areas in Figure 3b).[77] These are composed of approximately 2-4 graphene layers. For NGC1500, the graphene layers become more organized. More turbostratic domains composed of 5 to 7 graphene layers can be identified (cf. Figures 3c and 3d). Some graphene layers start to form hollow onion-like structures (see the green circle in Figure 3d).[77,78] These onion-like structures are even more visible for NGC2000 and NGC2500 (green areas in Figures 3e to 3h). These onion-like structures actually are enclosed pores, in agreement with previous studies on similar compounds.[79,80] Moreover, the diameter of these hollow onion-like structures increases as the pyrolysis temperature increases (from about 3 nm for NGC1500 to about 4 nm for NGC2000 and about 5 nm for NGC2500). As a consequence, the micropore size in the core is also increasing. For NGC2000 and NGC2500, the turbostratic domains are composed of approximately 5 to 10 graphene layers and their lateral size increases. These observations are in agreement with those made from Raman spectroscopy and XRD results: the average lateral size of the graphitic domains L_a increases and the structure of the NGC becomes more ordered as the pyrolysis temperature increases. The interlayer spacing was also determined from the TEM images of the four samples. These enable the evaluation of the interlayer distance $d_{(002)}$ (cf. Table 1). The same evolution than that from XRD was observed: the structure of the NGC evolves toward a more ordered structure with an interlayer distance that goes from 0.382 nm for NGC1000 to 0.352 nm for NGC2000 and NGC2500.

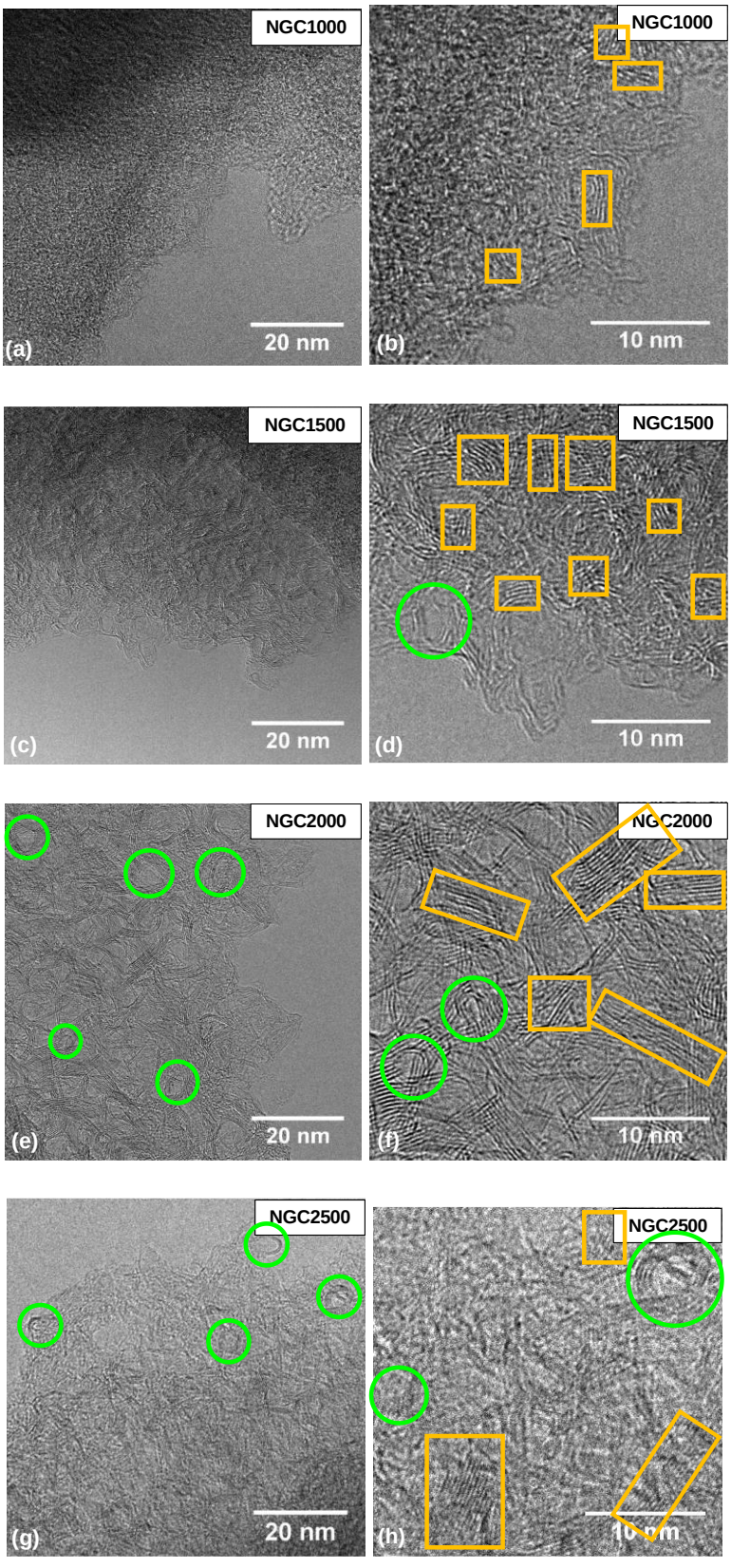

Fig. 3. TEM images for: (a) and (b) NGC1000, (c) and (d) NGC1500, (e) and (f) NGC2000, and (g) and (h) NGC2500. In orange: turbostratic domains (BSUs); in green: formation of onion-like nanostructures.

All the characterizations performed in this section lead to the same conclusion: when the pyrolysis temperature increases, the structure of the glassy carbons becomes more graphitic. To complete the study, the evolution of the textural properties (*i.e.*, the nature of the porosity) with the increase of the pyrolysis temperature was investigated.

Table 3 shows the evolution of A_{BET}. Low values were obtained for all NGCs (between 6 m^2/g (NGC1000) and 13 m^2/g (NGC1500)) and slightly decreases as the pyrolysis temperature increases above 1500 °C (from 13 m^2/g for NG1500 to 10 m^2/g for NGC2500). As the N_2 diffusion is slow at -196°C, this is not the most suitable gas to probe the narrow microporosity, i.e. ultra-micropores (pore diameter under 0.7 nm).[69] Therefore, H_2 ad/desorption at - 196 °C was then used to probe the porosity inaccessible to N_2. The molecule of H_2 has a diameter of 0.296 nm while more commonly used N_2 and CO_2 molecules have bigger diameters, 0.358 and 0.334 nm, respectively. Since gas diffusion is strongly dependent on temperature, the CO_2 adsorption at 0 °C is much faster than that of N_2 at - 196 °C, even though both molecules have similar diameters. Because the H_2 molecule has a smaller molecular diameter than the other gases, it can penetrate smaller pores and the range of PSD (Pose Size Distribution) analysis using this gas may be extended to a lower limit than the standard for N_2 + CO_2 dual analysis. Jagiello *et al*.[69] showed that a single H_2 isotherm might be sufficient for evaluating the carbon PSD in essentially ultra-microporous carbons, for which the H_2 uptake is higher than N_2 uptake. This N_2 + H_2 dual analysis showed that the materials have low porosity: the total pore volume determined using the NLDFT model decreases from 0.031 cm^3/g for NGC1000 to 0.018 cm^3/g for NGC1500, 0.0240 cm^3/g for NGC2000 and then slightly decreases to 0.016 cm^3/g for NGC2500 (Tables 3, S4 and S5).

Table 3. Textural parameters obtained by gas ad/desorption, He pycnometry and Small Angle X-Ray Scattering (SAXS) for NGC pyrolyzed at different temperatures.

	N_2 adsorption	N_2 adsorption and H_2 adsorption at -196°C				He pycnometry	SAXS	
Sample	**A_{BET} (m^2/g)[a]**	**S_{NLDFT} (m^2/g)[b]**	**V_μ (cm^3/g)[b]**	**V_{meso} (cm^3/g)[b]**	**V_{tot} (cm^3/g)[b]**	**Density (g/cm^3)[c]**	**V_{pores} (cm^3/g)[d]**	**Pore size (nm)[d]**
NGC1000	6	71	0.026 (84.0 %)	0.005 (16.0 %)	0.031	2.10 ± 0.01	0.114	0.70
NGC1500	13	20	0.006 (34.9 %)	0.012 (65.1 %)	0.018	1.54 ± 0.01	0.319	1.21
NGC2000	11	31	0.012 (50.0 %)	0.012 (50.0 %)	0.024	1.50 ± 0.01	1.114	1.53
NGC2500	10	14	0.004 (26.8 %)	0.012 (73.2 %)	0.016	1.53 ± 0.01	0.804	1.30

[a] Parameters calculated from N_2 isotherms at -196 °C: A_{BET}, area calculated by applying the BET model;

[b] Parameters calculated from the 2D-NLDFT HS model [69] using N_2 and H_2 isotherms at -196 °C: S_{NLDFT}, total specific surface area; V_μ, micropore volume (w < 2 nm); $V_{meso} = V_{tot} - V_\mu$, mesopore volume (2 nm < w < 50 nm); V_{tot}, total pore volume;

[c] Parameters obtained from He pycnometry

[d] Parameters obtained from Small Angle X-Ray Scattering (SAXS).

The evolution of the skeletal density of the materials was probed by He pycnometry (cf. Table 3). When the pyrolysis temperature increases, the skeletal density of the NGCs decreases from 2.10 g/cm^3 for NGC1000 to 1.54 g/cm^3 for NGC1500 and then remains quite stable around 1.5 g/cm^3 (1.50 g/cm^3 for NGC2000 and 1.53 g/cm^3 for NGC2500). For NGC1000, the skeletal density determined by He pycnometry 2.10 g/cm^3 matches the structural density for this type of sample obtained from XRD data as described in [70] (Table S6), meaning that all the micropores are accessible to He gas. On the contrary, for pyrolysis temperatures above 1500 °C, the lower density demonstrates that the porosity becomes inaccessible to He. In view of the results obtained for the characterization of porosity using both N_2 and H_2 as molecular probes, and the observations made from He pycnometry, it appears that the NGCs have a low pore

volume accessible to gases. Thus, SAXS was performed in order to probe the closed porosity (cf. Figure S5 and Table 3).

SAXS showed that, as the pyrolysis temperature increases, the pore volume in the NGCs increases significantly: from 12 % at 1000 °C to more than 30 % above 1500 °C (cf. Figure 4a and Table S6). The pore volume determined by SAXS is higher than that determined by gas ad/desorption: respectively 0.114 cm^3/g vs. 0.031 cm^3/g for NGC1000, 0.319 cm^3/g vs. 0.018 cm^3/g for NGC1500, 1.114 cm^3/g vs. 0.024 cm^3/g for NGC2000 and 0.863 cm^3/g vs. 0.016 cm^3/g for NGC2500. Moreover, the Specific Surface Area (SSA) determined by SAXS increases from 493 m^2/g for NGC1000 to 2190 m^2/g for NGC2000 and then decreases to 1851 m^2/g for NGC2500 (cf. Table S6). These pore volumes and SSA values are similar to what has been previously reported for HCs and GCs.[70] Higher pore volume and similarly high surface area values, several orders of magnitude higher than those obtained by gas ad/desorption, show that the high porosity of these materials is mainly closed and inaccessible to gases. The evolution of SSA can be explained by the evolution of the pore size from 0.70 nm for NGC1000 to 1.53 nm for NGC2000 and then its decrease to 1.30 nm for NGC2500. The pore network also becomes denser above 1500 °C, with the pore-to-pore distance decreasing from 9.05 nm for NGC1500 to 7.35 nm for NGC2500 (cf. Figure 4b and Table S6). Interestingly, NGC2000 was observed to have the highest SSA value and the lowest skeletal density.

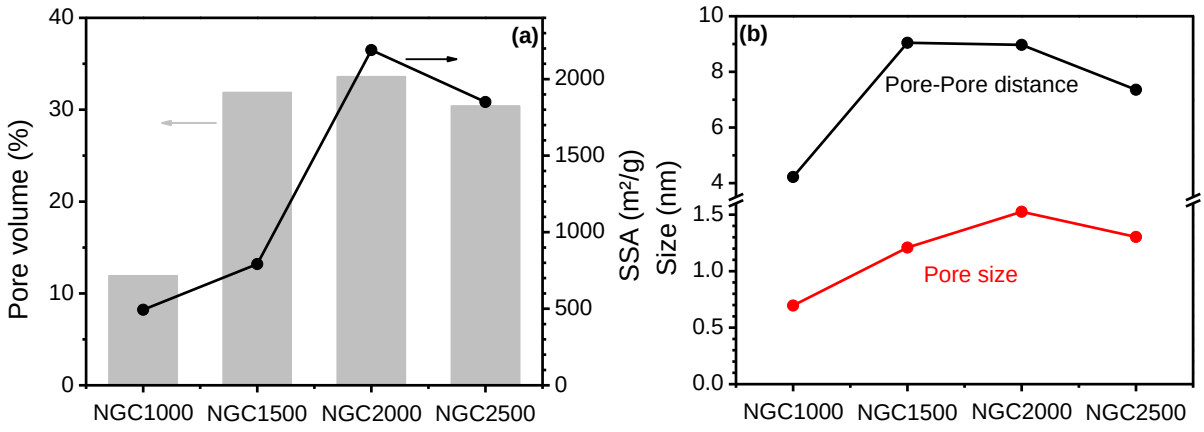

Fig. 4. Evolution of (a) pore volume, specific surface area (SSA), (b) pore size and pore-pore distance determined by SAXS for the NGCs.

3.1.2. Electrochemical performances

The electrochemical performances of the non-graphitizing carbons (NGC) were investigated by galvanostatic cycling in half-cell configuration with metallic sodium as counter and reference electrode. Figure 5 shows the first cycles obtained at a current rate of C/20 (18.6 mA/g_{carbon}) and a voltage range of 0-2.5 V (vs Na^+/Na). The electrochemical profiles can be divided into two parts: the sloping part between 2.5 V and 0.1 V (vs Na^+/Na) and the plateau below 0.1 V (vs Na^+/Na).

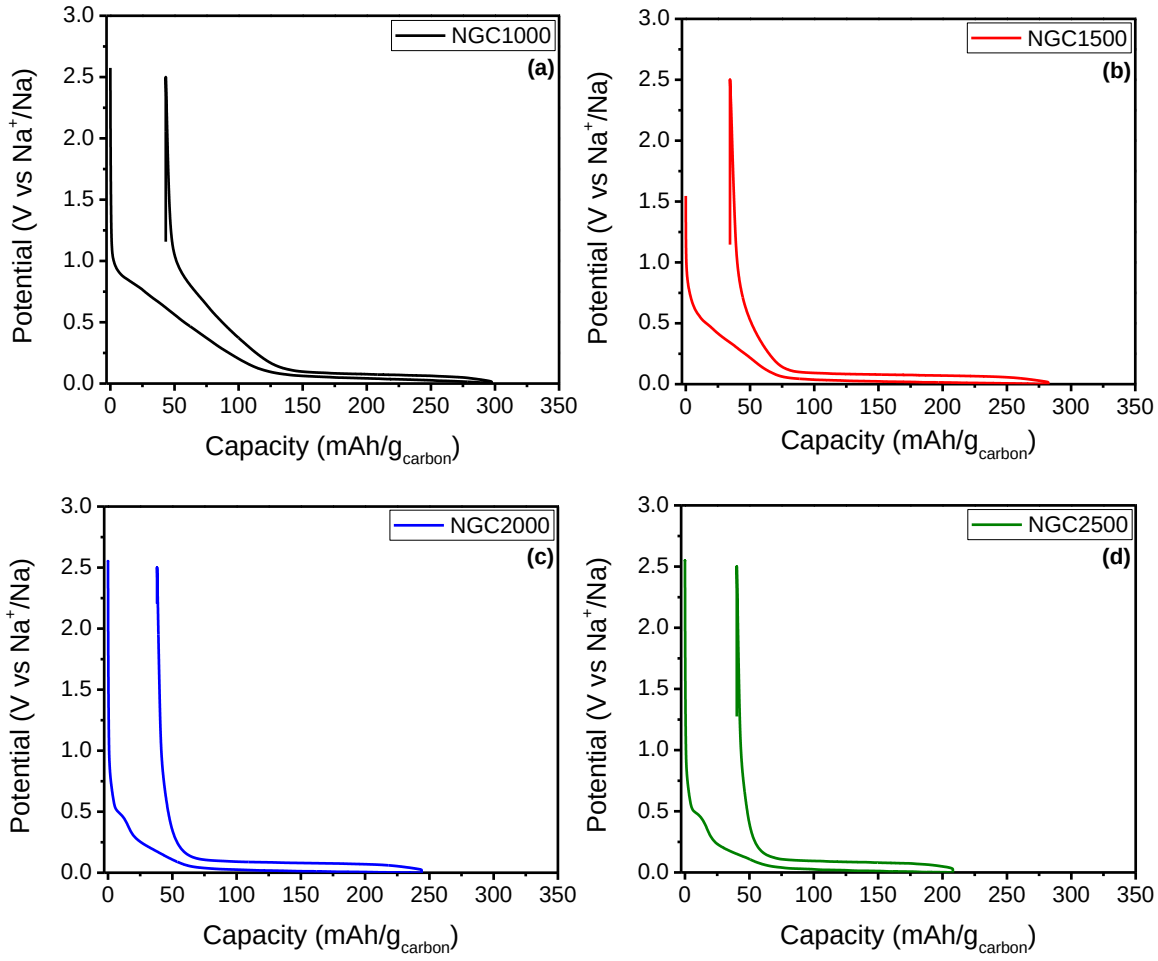

Fig. 5. First galvanostatic cycles at C/20 of (a) NGC1000, (b) NGC1500, (c) NGC2000 and (d) NGC2500.

The galvanostatic profiles for NGC1000 and NGC1500 are quite different from those of NGC2000 and NGC2500. For the lowest pyrolysis temperatures (*i.e*, 1000 °C and 1500 °C), the sloping part is clearly visible, while for the highest pyrolysis temperatures (*i.e.*, 2000 °C

and 2500 °C), it has completely disappeared upon charging. The voltage hysteresis between charge and discharge gradually increases from 0.03 V for NGC1000 to 0.07 V for NGC2500.

For the two samples treated at 2000 and 2500 °C, the galvanostatic profiles exclusively show a plateau at low voltage with a plateau capacity around 177 mAh/g for NGC2000 and 136 mAh/g for NGC2500 (Table 4). Moreover, the formation of Solid-Electrolyte Interphase (SEI) is very well seen for these two latter NGCs, with a visible plateau around 0.5 V vs Na^+/Na corresponding to the electrolyte decomposition of DMC on graphite-like structures [35] (cf. Figure 5). In terms of performance, the Coulombic efficiency at the first cycle (CE 1st) first increases to its maximum of 88% for NGC1500, then decreases as the pyrolysis temperature increases (see Table 4). At the same time, the reversible capacity decreases with increasing pyrolysis temperature: from ~ 250 mAh/g for NGC1000 to ~ 146 mAh/g for NGC2500, respectively (see Table 4). This decrease of the reversible capacity with the increase of the pyrolysis temperature is due to the disappearance of the sloping part for the samples pyrolyzed at 2000 °C and 2500 °C, and is also related to the increase of the polarization with the pyrolysis temperature, as mentioned at the end of the previous paragraph.

Table 4. Electrochemical performances of non-graphitizing carbons pyrolyzed at different temperatures.

Sample	**NGC1000**	**NGC1500**	**NGC2000**	**NGC2500**
Irreversible capacity (mAh/g_{carbon})	42 ± 2 (14%)	35 ± 1 (13%)	34 ± 3 (15%)	39 ± 1 (21%)
Sloping capacity (mAh/g_{carbon})	77 ± 3 (26%)	30 ± 1 (11%)	15 ± 7 (7%)	10 ± 1 (5%)
Plateau capacity (mAh/g_{carbon})	174 ± 2 (59%)	212 ± 7 (77%)	177 ± 23 (78%)	136 ± 26 (74%)
Total capacity first discharge (mAh/g_{carbon})	293 ± 7 (100%)	277 ± 7 (100%)	226 ± 26 (100%)	185 ± 28 (100%)
Rev. capacity (mAh/g_{carbon})	251 ± 5	242 ± 8	192 ± 29	146 ± 27
CE 1st (%)	86 ± 1	88 ± 1	85 ± 3	79 ± 3

The disappearance of the sloping part on NGC2000 and NGC2500 is interesting for the mechanistic understanding of sodium storage in NGC,[81] as only the contribution of sodium

storage over the plateau will be investigated. Due to the large differences in terms of structure and galvanostatic profiles between NGC1000 and NGC2500, we focused in the following on these two pyrolysis temperatures in order to study in more detail the phenomena occurring during sodiation of the materials.

3.2. *Mechanistic studies on sodium storage in NGC by in situ Raman spectroscopy*

To investigate the mechanism of sodium storage in NGC, *in situ* Raman spectroscopy was performed using three wavelengths 532 nm, 633 nm and 780 nm. The different wavelengths allow probing different depths of the sample and, as described in section 3.1.1., better separation of the D and G bands since the position of the D band depends on the laser energy (*i.e.*, the excitation wavelength). Besides, a fluorescence response of the electrolyte was observed for the excitation wavelengths of 532 nm and 633 nm (cf. Figure S6). Figures 6a, 6c, and 6e show the first-order Raman spectra for NGC1000 recorded during the first sodiation.

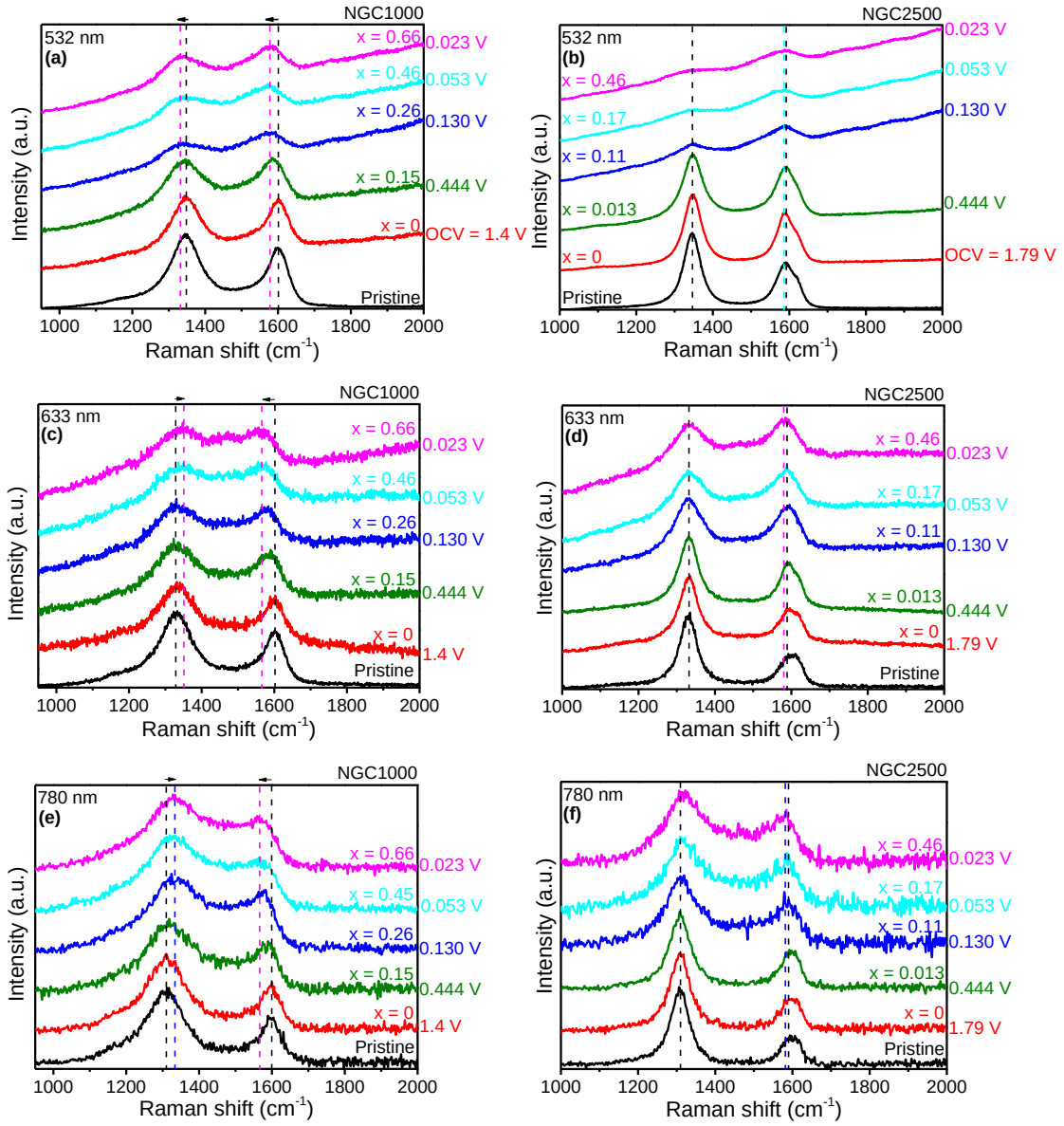

Fig. 6. First-order Raman spectra for NGC1000 at (a) 532 nm, (c) 633 nm and (e) 780 nm; and for NGC2500 at (b) 532 nm, (d) 633 nm and (f) 780 nm, recorded during the first sodiation.

For the three wavelengths, the position and width of the D and G bands of the NGC1000 electrode in contact with the electrolyte at open circuit voltage (OCV), remain similar to those of the pristine NGC1000 electrode. During the first discharge, an increase in the fluorescence signal is observed for the excitation wavelength of 532 nm, more particularly when the potential decreases from 0.444 V to 0.130 V. This could be attributed to the formation of the SEI as consequence of the degradation of the electrolyte on the electrode surface and causes the laser

to absorb for the mentioned wavelength.[65] The overlap between fluorescence and Raman scattering from the electrode surface makes analysis of the material difficult.[82]

Upon sodiation, both D and G bands broaden and the G band gradually shifts from ~ 1605 cm^{-1} to ~ 1567 cm^{-1}, ~ 1606 cm^{-1} to ~ 1565 cm^{-1} and ~ 1603 cm^{-1} to ~ 1561 cm^{-1} for the 532 nm, 633 nm and 780 nm excitation wavelengths, respectively. Contrary to studies performed using *operando* Raman analysis,[64,65] the D band remains visible and distinct. This may be due to the rearrangement of the structure during voltage relaxation. The G band shifts rapidly in the sloping part of the voltage profile (cf. Figure 7). An unexpected finding is that the position of the G band still shifts slightly as the voltage approaches the plateau region. The G band shift is similar for all three Raman excitation wavelengths: the slope of the linear fit is ~ 100 cm^{-1}/Na^+ inserted for the sloping part and ~30 cm^{-1}/Na^+ inserted for the plateau (cf. Table S7).

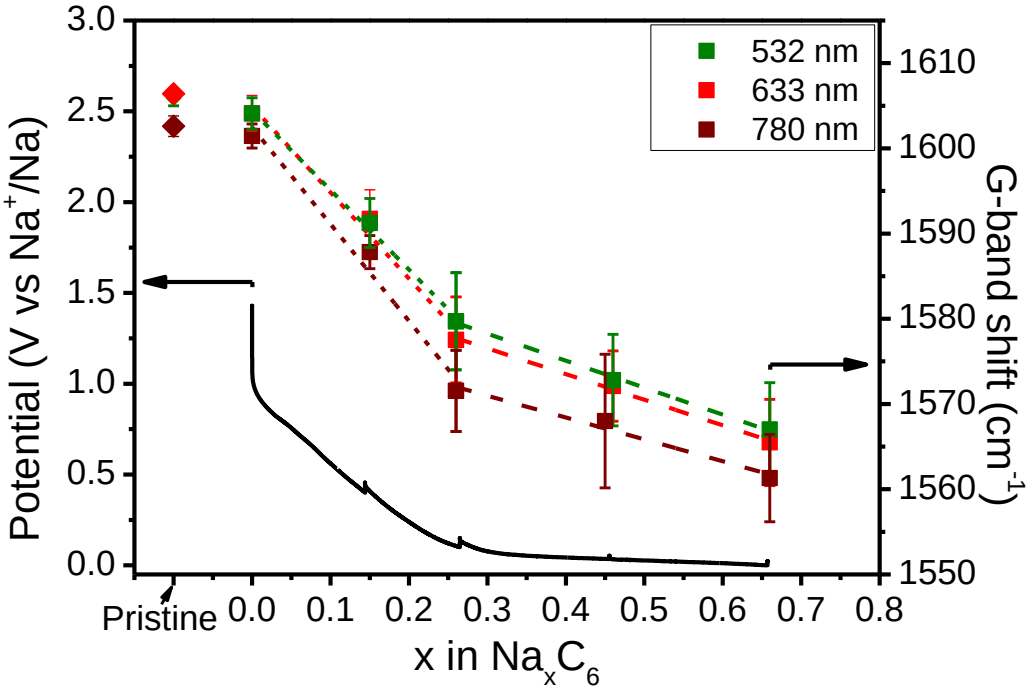

Fig. 7. Evolution of the G band position during the sodiation of NGC1000. Solid line: galvanostatic curve of NGC1000 at a rate of C/50; Dotted line: linear fit for the G band position on the sloping part; Dashed line: linear fit for the G band position on the plateau.

According to the literature, the shift of the G band is associated with a weakening of the in-plane C-C bond and an increase in the C-C distance.[35] Thus, the Raman analysis on

NGC1000 shows that the sloping part is associated to the intercalation of Na^+ between the graphene layers. This is in agreement with the observations made, using *operando* Raman spectroscopy, by Reddy *et al*.[64] and Weaving *et al*.[65] It is interesting to note in NGC1000 that intercalation also occurs during the low-voltage plateau, but is less pronounced than during the slope. This can explain the discrepancy between the previous reports, because if the focus is only on the low-voltage plateau, only intercalation will be observed, but this does not mean that this is where intercalation occurs predominantly.

Figures 6b, 6d and 6f show the first-order Raman spectra for NGC2500 recorded during the first sodiation. As with NGC1000, the D band remains visible and distinguishable while the D' band merges with the G band after the formation of the SEI. No significant change was observed in the D and G bands when the NGC2500 electrode was soaked in the electrolyte. The fluorescence signal increases drastically for Raman measurements with 532 nm. Both the D and G bands broaden upon sodiation, nevertheless, none of them shifts (cf. Figure S7). Thus, there is no intercalation of Na^+ between the graphene layers of NGC2500, which is consistent with the more ordered structure observed for NGC2500. The electrochemical profile of NGC2500 (cf. Figure 5d) shows a long plateau at low voltage and a negligible sloping part, thus, no intercalation occurs over the plateau. Moreover, as developed in Section 3.1.1, structural characterizations and elemental analysis showed that NGC2500 contains a very low amount of structural defects and heteroatoms while SAXS measurements revealed that NGC2500 has a developed closed microporosity. Therefore, the low-voltage plateau is associated with sodium filling of the micropores.

For these two samples, the mechanisms observed using in situ Raman spectroscopy are consistent with the root causes affecting the different storage behaviors of Na^+ in NGCs reported in the literature. To our knowledge, the root cause affecting intercalation seems to be mainly the interlayer distance $d_{(002)}$ in the turbostratic domains. As suggested by Dou et al. [6] in their review, the ideal $d_{(002)}$ value to intercalate Na ions is around 0.37-0.38 nm.[83] Such a distance facilitates the access of Na ions between the graphene layers.[84] Stevens and Dahn also suggested that the presence of hydrogen and other structural defects are responsible for the intercalation since there is an intimate correlation between structural defects and interlayer distance.[11] The root cause affecting pore filling seems to be mainly the pore size.[6,85] A pore diameter larger than 1 nm seems to be deleterious for Na filling inside the pores.

With a $d_{(002)}$ of 0.369-0.382 nm (see Table 1) and a pore diameter of 0.7 nm (see Table 3), the values of sloping and plateau capacities reported for NGC1000 (Table 4) seem to be

consistent with the mechanism revealed using in situ Raman spectroscopy. For NGC2500, the low value of $d_{(002)}$ (0.345-0.352 nm, see Table 1) making the intercalation of Na^+ between the graphene layers difficult could explain the disappearance of the sloping part (Figure 5d).

To optimize both Na^+ intercalation between graphene layers and pore filling, the ideal material would probably be one with a high micropore volume that contains many pores (open and closed), with a pore size of less than 1 nm and a homogenous distribution in the material. This ideal material should also have BSUs with an interlayer distance around 0.37 nm. In the context of this study, we could imagine that the material with the best performance should have the pore volume of NGC2000 (i.e. 1.114 cm^3/g) with the pore size and interlayer distance of NGC1000 (0.7 nm and 0.37 nm, respectively). Synthesis efforts are underway to achieve this duality.

4. Conclusions

The sodiation mechanism of commercial non-graphitizing carbons (NGC) prepared in the temperature range of 1000 °C to 2500 °C was thoroughly investigated. On the one hand, structural and textural characterizations showed that increasing the pyrolysis temperature leads to NGCs with a more ordered structure, containing fewer heteroatoms and structural defects and with a developed closed microporosity. Electrochemical tests revealed a deleterious effect of increasing the pyrolysis temperature on the electrochemical performance with a decrease in both reversible capacities and coulombic efficiency at the first cycle.

On the other hand, *in situ* Raman spectroscopy measurements were helpful in monitoring Na^+ intercalation between graphene layers. However, special attention should be paid to the selection of the appropriate wavelength of the Raman excitation laser to avoid fluorescence interference. When the galvanostatic profile presents a sloping part and a plateau region, as in the case of NGC1000 prepared at low pyrolysis temperature, *in situ* Raman analyses revealed that the intercalation of Na^+ between graphene layers occurred during the sloping part. When the galvanostatic profile shows only a flat plateau region, as in the case of NGC2500, no intercalation of Na^+ between graphene layers was observed and the low voltage plateau can be associated with sodium filling of the micropores. In the framework of this study,

a clear sodiation mechanism was identified but the universal nature of this mechanism is currently further investigated on other non-graphitizing carbons obtained from other precursors.

Acknowledgments

This work was supported by the French Ministry of Higher Education, Research and Innovation (Ministère de l'Enseignement Supérieur, de la Recherche et de l'Innovation (MESRI)). S. ADACH (L2CM, Nancy) is thanked for the elemental analysis of the glassy carbons. M. JAUREGUI is thanked for her support for SAXS measurements and SAXS data reduction. D. SAUREL is grateful for the funding provided by the Agencia Estatal de Investigación (AEI) through project PID2019-107468RB-C22.

References

[1] IPCC Working Group I, V. Masson-Delmotte, P. Zhai, A. Pirani, S.L. Connors, C. Péan, S. Berger, et al., Climate change 2021 - The physical science basis - Summary for policymakers, Cambridge University Press (2021) 3−32, Cambridge, UK and New York, NY, USA, doi: 10.1017/9781009157896.001.

[2] IPCC Working Group II, H.-O. Pörtner, D.C. Roberts, M. Tignor, E.S. Poloczanska, K. Mintenbeck, A. Alegría, et al., Climate change 2022 - Impacts, adaptation and vulnerability - Summary for policymakers, Cambridge University Press (2022) 3-33, Cambridge, UK and New York, NY, USA, doi:10.1017/9781009325844.001.

[3] IPCC Working Group III, P.R. Shukla, J. Skea, R. Slade, A. Al Khourdajie, R. van Diemen, D. McCollum, et al., Climate change 2022 - Mitigation of climate change - Summary for policymakers, Cambridge University Press (2022), Cambridge, UK and New York, NY, USA, doi: 10.1017/9781009157926.001.

[4] A. Kalair, N. Abas, M.S. Saleem, A.R. Kalair, N. Khan, Role of energy storage systems in energy transition from fossil fuels to renewables, Energy Storage. 3 (2021) 1–27. https://doi.org/10.1002/est2.135.

[5] P.A. Østergaard, N. Duic, Y. Noorollahi, S.A. Kalogirou, Recent advances in renewable energy technology for the energy transition, Renew. Energy. 179 (2021) 877–884. https://doi.org/10.1016/j.renene.2021.07.111.

[6] X. Dou, I. Hasa, D. Saurel, C. Vaalma, L. Wu, D. Buchholz, et al., Hard carbons for sodium-ion batteries: Structure, analysis, sustainability, and electrochemistry, Mater. Today. 23 (2019) 87–104. https://doi.org/10.1016/j.mattod.2018.12.040.

[7] S. Alvin, D. Yoon, C. Chandra, H.S. Cahyadi, J.H. Park, W. Chang, et al., Revealing sodium ion storage mechanism in hard carbon, Carbon 145 (2019) 67–81. https://doi.org/10.1016/j.carbon.2018.12.112.

[8] D. Saurel, B. Orayech, B. Xiao, D. Carriazo, X. Li, From charge storage mechanism to performance: A roadmap toward high specific energy sodium-ion batteries through carbon anode optimization, Adv. Energy Mater. 1703268 (2018) 1–33. https://doi.org/10.1002/aenm.201703268.

[9] C. Bommier, T.W. Surta, M. Dolgos, X. Ji, New mechanistic insights on Na-ion storage in non-graphitizable carbon, Nano Lett. 15 (2015) 5888–5892. https://doi.org/10.1021/acs.nanolett.5b01969.

[10] E. Goikolea, V. Palomares, S. Wang, I. Ruiz de Larramendi, X. Guo, G. Wang, et al., Na-ion Batteries - Approaching old and new challenges, Adv. Energy Mater. 10, 2002055 (2020) 1–21. https://doi.org/10.1002/aenm.202002055.

[11] D.A. Stevens, J.R. Dahn, The mechanisms of lithium and sodium insertion in carbon materials, J. Electrochem. Soc. 148 (2001) A803-A811. https://doi.org/10.1149/1.1379565.

[12] N. Yabuuchi, K. Kubota, M. Dahbi, S. Komaba, Research development on sodium-ion batteries, Chem. Rev. 114 (2014) 11636–11682. https://doi.org/10.1021/cr500192f.

[13] Y. Liu, B. V. Merinov, W.A. Goddard, Origin of low sodium capacity in graphite and generally weak substrate binding of Na and Mg among alkali and alkaline earth metals, Proc. Natl. Acad. Sci. USA 113 (2016) 3735–3739. https://doi.org/10.1073/pnas.1602473113.

[14] H. Pan, X. Lu, X. Yu, Y.S. Hu, H. Li, X.Q. Yang, et al., Sodium storage and transport properties in layered $Na_2Ti_3O_7$ for room-temperature sodium-ion batteries, Adv. Energy Mater. 3 (2013) 1186–1194. https://doi.org/10.1002/aenm.201300139.

[15] P. Senguttuvan, G. Rousse, V. Seznec, J.-M. Tarascon, M.R. Palacín, $Na_2Ti_3O_7$: Lowest voltage ever reported oxide insertion electrode for sodium-ion batteries, Chem. Mater.

23 (2011) 4109-4111. https://doi.org/10.1021/cm202076g.

[16] S. Hariharan, K. Saravanan, P. Balaya, α-MoO_3: A high performance anode material for sodium-ion batteries, Electrochem. Commun. 31 (2013) 5–9. https://doi.org/10.1016/j.elecom.2013.02.020.

[17] Q. Sun, Q.Q. Ren, H. Li, Z.W. Fu, High capacity Sb_2O_4 thin film electrodes for rechargeable sodium battery, Electrochem. Commun. 13 (2011) 1462–1464. https://doi.org/10.1016/j.elecom.2011.09.020.

[18] D. Su, H.J. Ahn, G. Wang, SnO_2@graphene nanocomposites as anode materials for Na-ion batteries with superior electrochemical performance, Chem. Commun. 49 (2013) 3131–3133. https://doi.org/10.1039/c3cc40448j.

[19] G.M. Tomboc, Y. Wang, H. Wang, J. Li, K. Lee, Sn-based metal oxides and sulfides anode materials for Na ion battery, Energy Storage Mater. 39 (2021) 21–44. https://doi.org/10.1016/j.ensm.2021.04.009.

[20] Y. Xu, Y. Zhu, Y. Liu, C. Wang, Electrochemical performance of porous carbon/tin composite anodes for sodium-ion and lithium-ion batteries, Adv. Energy Mater. 3 (2013) 128–133. https://doi.org/10.1002/aenm.201200346.

[21] J. Qian, Y. Chen, L. Wu, Y. Cao, X. Ai, H. Yang, High capacity Na-storage and superior cyclability of nanocomposite Sb/C anode for Na-ion batteries, Chem. Commun. 48 (2012) 7070–7072. https://doi.org/10.1039/c2cc32730a.

[22] L. Xiao, Y. Cao, J. Xiao, W. Wang, L. Kovarik, Z. Nie, et al., High capacity, reversible alloying reactions in SnSb/C nanocomposites for Na-ion battery applications, Chem. Commun. 48 (2012) 3321–3323. https://doi.org/10.1039/c2cc17129e.

[23] Y. Park, D.S. Shin, S.H. Woo, N.S. Choi, K.H. Shin, S.M. Oh, et al., Sodium terephthalate as an organic anode material for sodium ion batteries, Adv. Mater. 24 (2012) 3562–3567. https://doi.org/10.1002/adma.201201205.

[24] L. Zhao, J. Zhao, Y.S. Hu, H. Li, Z. Zhou, M. Armand, et al., Disodium terephthalate ($Na_2C_8H_4O_4$) as high-performance anode material for low-cost room-temperature sodium-ion battery, Adv. Energy Mater. 2 (2012) 962–965. https://doi.org/10.1002/aenm.201200166.

[25] A. Choi, Y.K. Kim, T.K. Kim, M.S. Kwon, K.T. Lee, H.R. Moon, 4,4′-Biphenyl-

dicarboxylate sodium coordination compounds as anodes for Na-ion batteries, J. Mater. Chem. A. 2 (2014) 14986–14993. https://doi.org/10.1039/c4ta02424a.

[26] Q. Zhao, Y. Lu, J. Chen, Advanced organic electrode materials for rechargeable sodium-ion batteries, Adv. Energy Mater. 7, 1601792 (2017) 2-22. https://doi.org/10.1002/aenm.201601792.

[27] V.A. Oltean, S. Renault, M. Valvo, D. Brandell, Sustainable materials for sustainable energy storage: Organic Na electrodes, Materials (Basel). 9, 142 (2016). https://doi.org/10.3390/ma9030142.

[28] H.S. Moon, J.H. Lee, S. Kwon, I.T. Kim, S.G. Lee, Mechanisms of Na adsorption on graphene and graphene oxide: density functional theory approach, Carbon Lett. 16 (2015) 116–120. https://doi.org/10.5714/CL.2015.16.2.116.

[29] J. Wan, F. Shen, W. Luo, L. Zhou, J. Dai, X. Han, et al., In situ transmission electron microscopy observation of sodiation-desodiation in a long cycle, high-capacity reduced graphene oxide sodium-ion battery anode, Chem. Mater. 28 (2016) 6528–6535. https://doi.org/10.1021/acs.chemmater.6b01959.

[30] X.F. Luo, C.H. Yang, J.K. Chang, Correlations between electrochemical Na^+ storage properties and physiochemical characteristics of holey graphene nanosheets, J. Mater. Chem. A. 3 (2015) 17282–17289. https://doi.org/10.1039/c5ta03687a.

[31] W. Luo, Z. Jian, Z. Xing, W. Wang, C. Bommier, M.M. Lerner, et al., Electrochemically expandable soft carbon as anodes for Na-ion batteries, ACS Cent. Sci. 1 (2015) 516–522. https://doi.org/10.1021/acscentsci.5b00329.

[32] Z. Jian, C. Bommier, L. Luo, Z. Li, W. Wang, C. Wang, et al., Insights on the mechanism of Na-ion storage in soft carbon anode, Chem. Mater. 29 (2017) 2314–2320. https://doi.org/10.1021/acs.chemmater.6b05474.

[33] Y. Cao, L. Xiao, M.L. Sushko, W. Wang, B. Schwenzer, J. Xiao, et al., Sodium ion insertion in hollow carbon nanowires for battery applications, Nano Lett. 12 (2012) 3783–3787. https://doi.org/10.1021/nl3016957.

[34] D.A. Stevens, J.R. Dahn, High capacity anode materials for rechargeable sodium-ion batteries, J. Electrochem. Soc. 147 (2000) 1271-1273. https://doi.org/10.1149/1.1393348.

[35] S. Komaba, W. Murata, T. Ishikawa, N. Yabuuchi, T. Ozeki, T. Nakayama, et al., Electrochemical Na insertion and solid electrolyte interphase for hard-carbon electrodes and application to Na-ion batteries, Adv. Funct. Mater. 21 (2011) 3859–3867. https://doi.org/10.1002/adfm.201100854.

[36] A. Gomez-Martin, J. Martinez-Fernandez, M. Ruttert, M. Winter, T. Placke, J. Ramirez-Rico, Correlation of structure and performance of hard carbons as anodes for sodium ion batteries, Chem. Mater. 31 (2019) 7288–7299. https://doi.org/10.1021/acs.chemmater.9b01768.

[37] P. Liu, Y. Li, Y.S. Hu, H. Li, L. Chen, X. Huang, A waste biomass derived hard carbon as a high-performance anode material for sodium-ion batteries, J. Mater. Chem. A. 4 (2016) 13046–13052. https://doi.org/10.1039/c6ta04877c.

[38] A. Beda, C. Villevieille, P.L. Taberna, P. Simon, C. Matei Ghimbeu, Self-supported binder-free hard carbon electrodes for sodium-ion batteries: Insights into their sodium storage mechanisms, J. Mater. Chem. A. 8 (2020) 5558–5571. https://doi.org/10.1039/c9ta13189b.

[39] N. Daher, D. Huo, C. Davoisne, P. Meunier, R. Janot, Impact of pre-oxidation treatments on performances of pitch-based hard carbons for sodium-ion batteries, ACS Appl. Energy Mater. 3 (2020) 6501–6510. https://doi.org/10.1021/acsaem.0c00727.

[40] C. Bommier, W. Luo, W.Y. Gao, A. Greaney, S. Ma, X. Ji, Predicting capacity of hard carbon anodes in sodium-ion batteries using porosity measurements, Carbon 76 (2014) 165–174. https://doi.org/10.1016/j.carbon.2014.04.064.

[41] W. Luo, C. Bommier, Z. Jian, X. Li, R. Carter, S. Vail, et al., Low-surface-area hard carbon anode for Na-ion batteries via graphene oxide as a dehydration agent, ACS Appl. Mater. Interfaces. 7 (2015) 2626–2631. https://doi.org/10.1021/am507679x.

[42] J.K. Mathiesen, R. Väli, M. Härmas, E. Lust, J. Fold Von Bülow, K.M.Ø. Jensen, et al., Following the in-plane disorder of sodiated hard carbon through: Operando total scattering, J. Mater. Chem. A. 7 (2019) 11709–11717. https://doi.org/10.1039/c9ta02413a.

[43] C. Matei Ghimbeu, J. Górka, V. Simone, L. Simonin, S. Martinet, C. Vix-Guterl, Insights on the Na^+ ion storage mechanism in hard carbon: Discrimination between the porosity, surface functional groups and defects, Nano Energy. 44 (2018) 327–335.

https://doi.org/10.1016/j.nanoen.2017.12.013.

[44] V. Simone, A. Boulineau, A. de Geyer, D. Rouchon, L. Simonin, S. Martinet, Hard carbon derived from cellulose as anode for sodium ion batteries: Dependence of electrochemical properties on structure, J. Energy Chem. 25 (2016) 761–768. https://doi.org/10.1016/j.jechem.2016.04.016.

[45] A. Beda, P.L. Taberna, P. Simon, C. Matei Ghimbeu, Hard carbons derived from green phenolic resins for Na-ion batteries, Carbon 139 (2018) 248–257. https://doi.org/10.1016/j.carbon.2018.06.036.

[46] A. Kamiyama, K. Kubota, T. Nakano, S. Fujimura, S. Shiraishi, H. Tsukada, et al., High-capacity hard carbon synthesized from macroporous phenolic resin for sodium-ion and potassium-ion battery, ACS Appl. Energy Mater. 3 (2020) 135–140. https://doi.org/10.1021/acsaem.9b01972.

[47] Y. Sun, P. Lu, X. Liang, C. Chen, H. Xiang, High-yield microstructure-controlled amorphous carbon anode materials through a pre-oxidation strategy for sodium ion batteries, J. Alloys Compd. 786 (2019) 468–474. https://doi.org/10.1016/j.jallcom.2019.01.388.

[48] G. Hasegawa, K. Kanamori, N. Kannari, J.I. Ozaki, K. Nakanishi, T. Abe, Studies on electrochemical sodium storage into hard carbons with binder-free monolithic electrodes, J. Power Sources. 318 (2016) 41–48. https://doi.org/10.1016/j.jpowsour.2016.04.013.

[49] Y. Lu, C. Zhao, X. Qi, Y. Qi, H. Li, X. Huang, et al., Pre-oxidation-tuned microstructures of carbon anodes derived from pitch for enhancing Na storage performance, Adv. Energy Mater. 8, 1800108 (2018) 1–6. https://doi.org/10.1002/aenm.201800108.

[50] A. Beda, J.M. Le Meins, P.L. Taberna, P. Simon, C. Matei Ghimbeu, Impact of biomass inorganic impurities on hard carbon properties and performance in Na-ion batteries, Sustain. Mater. Technol. 26 (2020). https://doi.org/10.1016/j.susmat.2020.e00227.

[51] C. del M. Saavedra Rios, V. Simone, L. Simonin, S. Martinet, C. Dupont, Biochars from various biomass types as precursors for hard carbon anodes in sodium-ion batteries, Biomass and Bioenergy. 117 (2018) 32–37. https://doi.org/10.1016/j.biombioe.2018.07.001.

[52] C.D.M. Saavedra Rios, L. Simonin, A. De Geyer, C.M. Ghimbeu, C. Dupont, Unraveling the properties of biomass-derived hard carbons upon thermal treatment for a practical application in Na-ion batteries, Energies. 13, 3513 (2020). https://doi.org/10.3390/en13143513.

[53] J. Górka, C. Vix-Guterl, C. Matei Ghimbeu, Recent progress in design of biomass-derived hard carbons for sodium-ion batteries, C – Journal of carbon research. 2, 24 (2016). https://doi.org/10.3390/c2040024.

[54] H. Tonnoir, D. Huo, R.L.S. Canevesi, V. Fierro, A. Celzard, R. Janot, Tannin-based hard carbons as high-performance anode materials for sodium-ion batteries, Mater. Today Chem. 23 (2022) 100614. https://doi.org/10.1016/j.mtchem.2021.100614.

[55] L. Monconduit, L. Croguennec, Na-ion batteries, ISTE, WILEY, 2021, ISBN: 9781789450132.

[56] J.C. Lewis, B. Redfern, F.C. Cowlard, Vitreous carbon as a crucible material for semiconductors, Solid State Electron. 6 (1963) 251–254. https://doi.org/10.1016/0038-1101(63)90081-9.

[57] F.C. Cowlard, J.C. Lewis, Vitreous carbon - A new form of carbon, J. Mater. Sci. 2 (1967) 507–512. https://doi.org/10.1007/BF00752216.

[58] H. Appleby, F.C. Cowlard, United States Patent: 3626042, 1971.

[59] D.A. Stevens, J.R. Dahn, An in-situ small-angle X-ray scattering study of sodium insertion into a nanoporous carbon anode material within an operating electrochemical cell, J. Electrochem. Soc. 147, 12 (2000) 4428-4431. https://doi.org/10.1149/1.1394081.

[60] N. Sun, Z. Guan, Y. Liu, Y. Cao, Q. Zhu, H. Liu, et al., Extended “Adsorption–Insertion” Model: A New Insight into the Sodium Storage Mechanism of Hard Carbons, Adv. Energy Mater. 9 (2019) 1–14. https://doi.org/10.1002/aenm.201901351.

[61] J.M. Stratford, P.K. Allan, O. Pecher, A. Chater, C.P. Grey, Mechanistic insights into sodium storage in hard carbon anodes using local structure probes, Chem. Commun. 52 (2016) 12430–12433. https://doi.org/10.1039/C6CC06990H.

[62] S. Qiu, L. Xiao, M.L. Sushko, K.S. Han, Y. Shao, M. Yan, et al., Manipulating adsorption-insertion mechanisms in nanostructured carbon materials for high-efficiency sodium ion storage, Adv. Energy Mater. 7, 1700403 (2017) 1–11.

https://doi.org/10.1002/aenm.201700403.

[63] H. Au, H. Alptekin, A.C.S. Jensen, E. Olsson, C.A. O'Keefe, T. Smith, et al., A revised mechanistic model for sodium insertion in hard carbons, Energy Environ. Sci. 13 (2020) 3469–3479. https://doi.org/10.1039/d0ee01363c.

[64] M. Anji Reddy, M. Helen, A. Groß, M. Fichtner, H. Euchner, Insight into sodium insertion and the storage mechanism in hard carbon, ACS Energy Lett. 3 (2018) 2851–2857. https://doi.org/10.1021/acsenergylett.8b01761.

[65] J.S. Weaving, A. Lim, J. Millichamp, T.P. Neville, D. Ledwoch, E. Kendrick, et al., Elucidating the sodiation mechanism in hard carbon by operando Raman spectroscopy, ACS Appl. Energy Mater. 3 (2020) 7474–7484. https://doi.org/10.1021/acsaem.0c00867.

[66] M.M. Titirici, H. Alptekin, H. Au, A.C.S. Jensen, E. Olsson, M. Goktas, et al., Sodium storage mechanism investigations through structural changes in hard carbons, ACS Appl. Energy Mater. 3 (2020) 9918–9927. https://doi.org/10.1021/acsaem.0c01614.

[67] P. Mallet-Ladeira, Analyse multi-échelle de carbones pyrolytiques, PhD Thesis, Université Toulouse 3 Paul Sabatier, France, 2014.

[68] P. Mallet-Ladeira, P. Puech, C. Toulouse, M. Cazayous, N. Ratel-Ramond, P. Weisbecker, et al., A Raman study to obtain crystallite size of carbon materials: A better alternative to the Tuinstra-Koenig law, Carbon 80 (2014) 629–639. https://doi.org/10.1016/j.carbon.2014.09.006.

[69] J. Jagiello, J. Kenvin, C.O. Ania, J.B. Parra, A. Celzard, V. Fierro, Exploiting the adsorption of simple gases O_2 and H_2 with minimal quadrupole moments for the dual gas characterization of nanoporous carbons using 2D-NLDFT models, Carbon 160 (2020) 164–175. https://doi.org/10.1016/j.carbon.2020.01.013.

[70] D. Saurel, J. Segalini, M. Jauregui, A. Pendashteh, B. Daffos, P. Simon, et al., A SAXS outlook on disordered carbonaceous materials for electrochemical energy storage, Energy Storage Mater. 21 (2019) 162–173. https://doi.org/10.1016/j.ensm.2019.05.007.

[71] R.E. Franklin, The structure of graphitic carbons, Acta Crystallogr. 4 (1951) 253–261. https://doi.org/10.1107/s0365110x51000842.

[72] P. Puech, M. Kandara, G. Paredes, L. Moulin, E. Weiss-Hortala, A. Kundu, et al.,

Analyzing the Raman spectra of graphenic carbon materials from kerogens to nanotubes: What type of information can be extracted from defect bands?. C – Journal of carbon research. 5, 69 (2019). https://doi.org/10.3390/c5040069.

[73] A. Merlen, J.G. Buijnsters, C. Pardanaud, A guide to and review of the use of multiwavelength Raman spectroscopy for characterizing defective aromatic carbon solids: From graphene to amorphous carbons, Coatings 7, 153 (2017). https://doi.org/10.3390/coatings7100153.

[74] C. Thomsen, S. Reich, Double resonant Raman scattering in graphite, Phys. Rev. Lett. 85 (2000) 5214–5217. https://doi.org/10.1103/PhysRevLett.85.5214.

[75] L.G. Cançado, A. Jorio, E.H.M. Ferreira, F. Stavale, C.A. Achete, R.B. Capaz, et al., Quantifying defects in graphene via Raman spectroscopy at different excitation energies, Nano Lett. 11 (2011) 3190–3196. https://doi.org/10.1021/nl201432g.

[76] L.G. Cançado, K. Takai, T. Enoki, M. Endo, Y.A. Kim, H. Mizusaki, et al., General equation for the determination of the crystallite size La of nanographite by Raman spectroscopy, Appl. Phys. Lett. 88, 163106 (2006) 1–4. https://doi.org/10.1063/1.2196057.

[77] P.J.F. Harris, New perspectives on the structure of graphitic carbons, Crit. Rev. Solid State Mater. Sci. 30 (2005) 235–253. https://doi.org/10.1080/10408430500406265.

[78] P.J.F. Harris, A. Burian, S. Duber, High-resolution electron microscopy of a microporous carbon, Philos. Mag. Lett. 80 (2000) 381–386. https://doi.org/10.1080/095008300403512.

[79] K. Jurkiewicz, M. Pawlyta, D. Zygadło, D. Chrobak, S. Duber, R. Wrzalik, et al., Evolution of glassy carbon under heat treatment: Correlation structure–mechanical properties, J. Mater. Sci. 53 (2018) 3509–3523. https://doi.org/10.1007/s10853-017-1753-7.

[80] P.J.F. Harris, Structure of non-graphitizing carbons, Int. Mater. Rev. 42, 5 (1997) 206–218. https://doi.org/10.1179/imr.1997.42.5.206

[81] Y. Morikawa, S. Nishimura, R. Hashimoto, M. Ohnuma, A. Yamada, Mechanism of sodium storage in hard carbon: An X-ray scattering analysis, Adv. Energy Mater. 10, 1903176 (2020). https://doi.org/10.1002/aenm.201903176.

[82] L. Cabo-Fernandez, A.R. Neale, F. Braga, I. V. Sazanovich, R. Kostecki, L.J. Hardwick, Kerr gated Raman spectroscopy of $LiPF_6$ salt and $LiPF_6$-based organic carbonate electrolyte for Li-ion batteries, Phys. Chem. Chem. Phys. 21 (2019) 23833–23842. https://doi.org/10.1039/c9cp02430a.

[83] S. Qiu, L. Xiao, M.L. Sushko, K.S. Han, Y. Shao, M. Yan, et al., Manipulating Adsorption–Insertion Mechanisms in Nanostructured Carbon Materials for High-Efficiency Sodium Ion Storage, Adv. Energy Mater. 7 (2017) 1–11. https://doi.org/10.1002/aenm.201700403.

[84] P.C. Tsai, S.C. Chung, S.K. Lin, A. Yamada, Ab initio study of sodium intercalation into disordered carbon, J. Mater. Chem. A. 3 (2015) 9763–9768. https://doi.org/10.1039/c5ta01443c.

[85] H. Marsh, F. Rodriguez-Reinoso, Activated carbon, Elsevier Science and Technology Books (2006), https://doi.org/10.1016/B978-0-08-044463-5.X5013-4.

Highlights

- Hard and glassy carbons are synthesized at four different pyrolysis temperatures
- Materials characterizations are structural, textural and electrochemical
- Pyrolysis temperature dependence of structure, performance and Na storage mechanism
- Multi-wavelength Raman spectroscopy is used for structural and mechanistic studies
- *In situ* Raman spectroscopy shows intercalation-pore filling mechanism

Graphical Abstract